



Effects of the Central Mass Concentration on Bar Formation in Disk Galaxies

DAJEONG JANG ¹ AND WOONG-TAE KIM ^{1,2}¹*Department of Physics & Astronomy, Seoul National University, Seoul 08826, Republic of Korea*²*SNU Astronomy Research Center, Seoul National University, Seoul 08826, Republic of Korea*

ABSTRACT

While bars are common in disk galaxies, their formation conditions are not well understood. We use N -body simulations to study bar formation and evolution in isolated galaxies consisting of a stellar disk, a classical bulge, and a dark halo. We consider 24 galaxy models that are similar to the Milky Way but differ in the mass and compactness of the classical bulge and halo concentration. We find that the bar formation requires $(Q_{T,\min}/1.2)^2 + (\text{CMC}/0.05)^2 \lesssim 1$, where $Q_{T,\min}$ and CMC refers to the minimum value of the Toomre stability parameter and the central mass concentration, respectively. Bars tend to be stronger, longer, and rotate slower in galaxies with a less massive and less compact bulge and halo. All bars formed in our models correspond to slow bars. A model with the bulge mass of ~ 10 –20% of the disk under a concentrated halo produces a bar similar to the Milky-Way bar. We discuss our findings in relation to other bar formation criteria suggested by previous studies.

Keywords: Disk Galaxies (391), Milky Way Galaxy (1054), Galaxy Bulges (578), Galaxy Disks (589), Barred Spiral Galaxies (136), Galaxy Bars (2364)

1. INTRODUCTION

Bars are common in the universe. More than $\sim 60\%$ of disk galaxies in optical and near-infrared images are known to possess a weak or strong bar in the local universe (de Vaucouleurs 1963; Sellwood & Wilkinson 1993; Knapen et al. 2000; Whyte et al. 2002; Laurikainen et al. 2004; Marinova & Jogee 2007; Menéndez-Delmestre et al. 2007; Aguerri et al. 2009; Méndez-Abreu et al. 2012; Buta et al. 2015; Díaz-García et al. 2016, 2019). The fraction of barred disk galaxies decreases with redshift (Sheth et al. 2008; Melvin et al. 2014), with a tendency that more massive galaxies are more likely barred. Bar formation appears inhibited in dispersion-dominated galaxies and in halo-dominated galaxies at low redshift (Sheth et al. 2012). These indicate that the bar formation occurs preferentially in a late secular phase of galaxy formation when the disks become dynamically cold (Kraljic et al. 2012).

Theoretically, bar formation is due to gravitational instability of a rotationally-supported stellar disk (Toomre 1964): non-axisymmetric perturbations grow via swing

amplification and initially circular stellar orbits are deformed to elongated x_1 orbits that form and support a bar (see, e.g., Sellwood 2014). A number of simulations have shown that the presence of a dark halo affects the bar formation and evolution (Ostriker & Peebles 1973; Hohl 1976; Debattista & Sellwood 2000; Valenzuela & Klypin 2003; Holley-Bockelmann et al. 2005; Weinberg & Katz 2007). While the gravity of a halo tends to suppress the bar formation by reducing the relative strength of the disk’s self-gravity in equilibrium (Ostriker & Peebles 1973), angular momentum exchange between a bar and a live halo allows the former to grow longer and stronger (Athanassoula 2002). Also, the halo parameters such as the axial ratio (Athanassoula 2002; Athanassoula et al. 2013) and spin (Collier et al. 2018, 2019; Kataria & Shen 2022) lead to considerable changes in the bar evolution.

In addition to a halo, a classical bulge can also strongly affect the bar formation and evolution. Classical bulges are produced as a result of major/minor mergers during galaxy formation (Kauffmann et al. 1993; Baugh et al. 1996; Hopkins et al. 2009; Naab et al. 2014; Bournaud et al. 2007; Hopkins et al. 2010). Unlike halos, classical bulges are highly centrally concentrated and can thus stabilize the inner regions of disks, without affecting the outer regions much. Early studies found

that a strong bulge suppresses swing amplification by interrupting a feedback loop that transforms propagating trailing waves to leading ones (Sellwood 1980; Toomre 1981; Binney & Tremaine 2008), inhibiting bar formation (e.g., Saha & Elmegreen 2018; Kataria & Das 2018). Also, a live bulge can make a bar longer and stronger by removing angular momentum from the latter, just like a live halo (Sellwood 1980). A bar that forms can increase a central mass, for example, by driving gas inflows (e.g., Athanassoula 1992; Buta & Combes 1996; Kim et al. 2012), which in turns weakens or destroys the bar by disturbing bar-supporting x_1 orbits (e.g., Pfenniger & Norman 1990; Hasan et al. 1993; Norman et al. 1996; Shen & Sellwood 2004; Bournaud et al. 2005; Athanassoula et al. 2013).

While many numerical studies mentioned above are useful to understand the effects of a bulge and a halo on the bar formation and evolution, the quantitative conditions for bar-forming instability have still been under debate. Using numerical models with a fixed halo and a disk with surface density $\Sigma_d \propto R^{-1}$, Ostriker & Peebles (1973) suggested that bar formation requires

$$t_{\text{OP}} \equiv T/|W| > 0.14, \quad (1)$$

where T and W stand for the total rotational and gravitational potential energies of a galaxy, respectively. Using two-dimensional (2D) models with a fixed halo and an exponential disk, Efsthathiou et al. (1982) showed that a bar forms in galaxies with

$$\epsilon_{\text{ELN}} \equiv \frac{V_{\text{max}}}{(GM_d/R_d)^{1/2}} < 1.1, \quad (2)$$

where V_{max} , M_d , and R_d refer to the maximum rotational velocity, mass, and scale radius of the disk, respectively.

It is not until recent years that galaxy models for bar formation treat all three components (disk, bulge, and halo) as being live (Polyachenko et al. 2016; Salo & Laurikainen 2017; Saha & Elmegreen 2018; Fujii et al. 2018; Kataria & Das 2018, 2019; Kataria et al. 2020). In particular, Kataria & Das (2018) used self-consistent N -body simulations with differing bulge masses, and showed that bar formation requires that the ratio of the bulge to total radial force initially satisfies

$$\mathcal{F}_{\text{KD}} \equiv \frac{GM_b}{R_d V_{\text{tot}}^2} < 0.35, \quad (3)$$

where M_b is the bulge mass and V_{tot} is the total rotational velocity at $R = R_d$. Using three-component galaxy models with differing disk and bulge densities, Saha & Elmegreen (2018) argued that their models

evolve to barred galaxies provided

$$\mathcal{D}_{\text{SE}} \equiv \frac{\langle \rho_b \rangle}{\langle \rho_d \rangle} < \frac{1}{\sqrt{10}}, \quad (4)$$

where $\langle \rho_b \rangle$ and $\langle \rho_d \rangle$ are the mean densities of the bulge and disk, respectively, within the half-mass radius of the bulge.

The several different conditions given above imply that there has not been consensus regarding the quantitative criterion for bar formation. A part of the reason for the discrepancies in the proposed conditions may be that some models considered a fixed (rather than live) halo, and that some authors explored parameter space by fixing either bulge or halo parameters. Also, it is questionable whether the effects of the complicated physical processes (swing amplification and feedback loop) involved in the bar formation can be encapsulated by the single parameters given above. In this paper, we revisit the issue of bar formation by varying both bulge and halo parameters altogether. Our models will be useful to clarify what conditions are necessary to produce a bar when the mass and compactness of the bulge and halo vary. We will show that the two key elements that govern the bar formation are the minimum value of the Toomre stability parameter $Q_{T,\text{min}}$ and the central mass concentration (CMC), defined as the total galaxy mass inside the central 0.1 kpc relative to the total disk mass: bars form more easily in galaxies with smaller $Q_{T,\text{min}}$ and CMC. We also measure the strength, length, and pattern speed of the bars that form in our simulations and explore their dependence on the halo and bulge parameters.

This paper is organized as follows. In Section 2, we describe our galaxy models and numerical methods we employ. In Section 3, we present temporal changes of the bar properties such as bar strength, pattern speed, length, and angular momentum transfer from a disk to halo and bulge. In Section 4, we compare our numerical results with the previous bar formation conditions mentioned above, and propose the new conditions in terms of $Q_{T,\text{min}}$ and CMC. We also use our numerical model to constrain the classical bulge of the Milky Way. Finally, we conclude our work in Section 5.

2. GALAXY MODEL AND METHOD

2.1. Galaxy Models

To study the effects of spheroidal components on the bar formation and evolution in disk galaxies, we consider Milky Way-like, isolated galaxies. Our galaxy models are three dimensional (3D), consisting of a dark mat-

Table 1. Model parameters and various dimensionless quantities of the initial galaxy models

Model	a_h (kpc)	M_b/M_d	a_b (kpc)	$Q_{T,\min}$	CMC	t_{OP}	ϵ_{ELN}	\mathcal{F}_{KD}	\mathcal{D}_{SE}
(1)	(2)	(3)	(4)	(5)	(6)	(7)	(8)	(9)	(10)
C00	30	0.0	0.4	1.062	0.04×10^{-2}	0.449	0.89	0.0	0.0
C05	30	0.05	0.4	1.079	0.24×10^{-2}	0.449	0.90	0.10	0.67
C10	30	0.1	0.4	1.085	0.44×10^{-2}	0.447	0.91	0.19	1.30
C20	30	0.2	0.4	1.110	0.84×10^{-2}	0.446	0.92	0.33	2.60
C30	30	0.3	0.4	1.140	1.22×10^{-2}	0.445	0.94	0.44	3.90
C40	30	0.4	0.4	1.164	1.62×10^{-2}	0.444	0.95	0.52	5.20
L00	40	0.0	0.4	0.954	0.04×10^{-2}	0.442	0.80	0.0	0.0
L05	40	0.05	0.4	0.961	0.24×10^{-2}	0.441	0.81	0.12	0.64
L10	40	0.1	0.4	0.975	0.44×10^{-2}	0.440	0.82	0.22	1.30
L20	40	0.2	0.4	1.000	0.84×10^{-2}	0.439	0.84	0.37	2.61
L30	40	0.3	0.4	1.023	1.24×10^{-2}	0.438	0.86	0.49	3.91
L40	40	0.4	0.4	1.046	1.64×10^{-2}	0.437	0.89	0.58	5.19
L50	40	0.5	0.4	1.056	2.06×10^{-2}	0.436	0.99	0.64	6.05
C05c	30	0.05	0.2	1.082	0.58×10^{-2}	0.447	0.90	0.10	3.01
C10c	30	0.1	0.2	1.086	1.16×10^{-2}	0.446	0.91	0.18	5.76
C20c	30	0.2	0.2	1.106	2.26×10^{-2}	0.442	0.92	0.32	11.30
C30c	30	0.3	0.2	1.127	3.34×10^{-2}	0.439	1.07	0.42	16.80
C40c	30	0.4	0.2	1.158	4.40×10^{-2}	0.437	1.23	0.50	22.21
L05c	40	0.05	0.2	0.961	0.58×10^{-2}	0.439	0.81	0.12	2.89
L10c	40	0.1	0.2	0.972	1.16×10^{-2}	0.438	0.82	0.21	5.72
L20c	40	0.2	0.2	0.999	2.26×10^{-2}	0.435	0.88	0.36	11.28
L30c	40	0.3	0.2	1.024	3.38×10^{-2}	0.432	1.07	0.46	16.84
L40c	40	0.4	0.2	1.049	4.48×10^{-2}	0.430	1.23	0.54	22.06
L50c	40	0.5	0.2	1.049	5.62×10^{-2}	0.428	1.38	0.59	25.53

ter halo, a classical bulge, a stellar disk, and a central supermassive black hole.

For the stellar disk, we adopt the exponential-secant hyperbolic density distribution

$$\rho_d(R, z) = \frac{M_d}{4\pi z_d R_d^2} \exp\left(-\frac{R}{R_d}\right) \text{sech}^2\left(\frac{z}{z_d}\right), \quad (5)$$

where R is the cylindrical radius, R_d is the disk scale radius, z_d is the disk scale height, and M_d is the total disk mass. We fix $R_d = 3$ kpc, $z_d = 0.3$ kpc, and $M_d = 5 \times 10^{10} M_\odot$, similar to the Milky Way (Bland-Hawthorn & Gerhard 2016, Helmi 2020). Initially, we set the velocity anisotropy to $f_R \equiv \sigma_R^2/\sigma_z^2 = 2.0$, where σ_R and σ_z refer to the velocity dispersions of the disk particles in the radial and vertical directions, respectively. We note that f_R increases with time as the disk evolves to form a bar, becoming similar to the observed value of $f_R \sim 4$ near the solar neighborhood (e.g.,

Sharma et al. 2014; Guiglion et al. 2015; Katz et al. 2018).

For both halo and classical bulge, we take the Hernquist (1990) profile

$$\rho(r) = \frac{M}{2\pi} \frac{a}{r(r+a)^3}, \quad (6)$$

where $r = (R^2 + z^2)^{1/2}$ is the spherical radius, and M and a denote the mass and the scale radius of each component, respectively. For the halo, we fix its mass to $M_h = 1.35 \times 10^{12} M_\odot = 26M_d$ and consider two scale radii: a centrally concentrated halo with $a_h = 30$ kpc and a less concentrated halo with $a_h = 40$ kpc, which we term C and L series, respectively. For the bulge, we vary both mass $M_b = (0-0.5)M_d$ and scale radius a_b between 0.2 to 0.4 kpc. We place a supermassive black hole with mass $M_{BH} = 4 \times 10^6 M_\odot$ at the galaxy center.

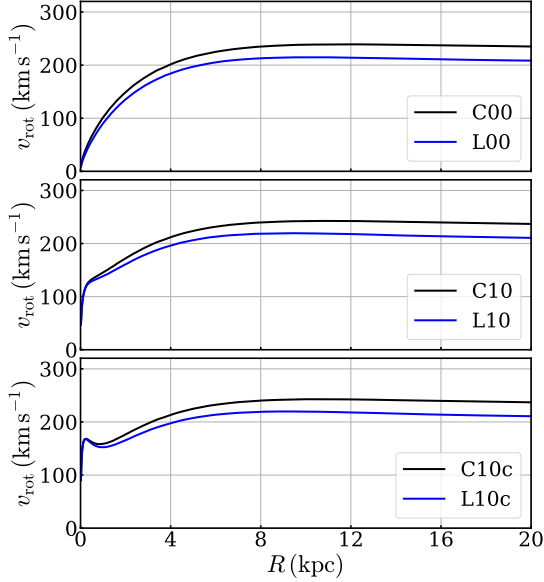


Figure 1. Radial distributions of the total rotational velocity v_{rot} for models C00, L00 (top), C10, L10 (middle), and C10c, L10c (bottom). A more massive and compact bulge increase v_{rot} at small R . Models in the C series have higher v_{rot} , by $\sim 20 \text{ km s}^{-1}$ on average, than in the L series.

Table 1 lists the names and initial parameters of all models. Column (1) gives the model names. Column (2) gives the scale radius of the halo, while Columns (3) and (4) list the bulge mass relative to the disk mass and the bulge scale radius, respectively. The prefix C and L in the model names stand for the centrally concentrated and less concentrated halo, respectively. The number after the prefix denotes the bulge mass relative to the total disk mass. The postfix c implies a compact bulge: the models with and without the postfix have $a_b = 0.2 \text{ kpc}$ and 0.4 kpc , respectively. For example, model L20c has a less-concentrated halo with $a_h = 40 \text{ kpc}$ and a compact bulge with $M_b = 0.2M_d$ and $a_b = 0.2 \text{ kpc}$. Column (5) lists the minimum value of the Toomre stability parameter. Column (6) lists the CMC. Columns (7)–(10) give the values for the quantities defined in Equations (1) to (4). We take model C10 as our fiducial model.

Figure 1 plots the radial distributions of the total rotational velocity v_{rot} for selected models. The black and blue lines correspond to the models in the C and L series, respectively. It is apparent that increasing the bulge mass enhances the rotational velocity. Models with a compact bulge have higher rotational velocity in the inner regions with $R \lesssim a_b$. At $R \lesssim 20 \text{ kpc}$, models in the C series have larger v_{rot} , by $\sim 20 \text{ km s}^{-1}$ on average, than the L series counterparts.

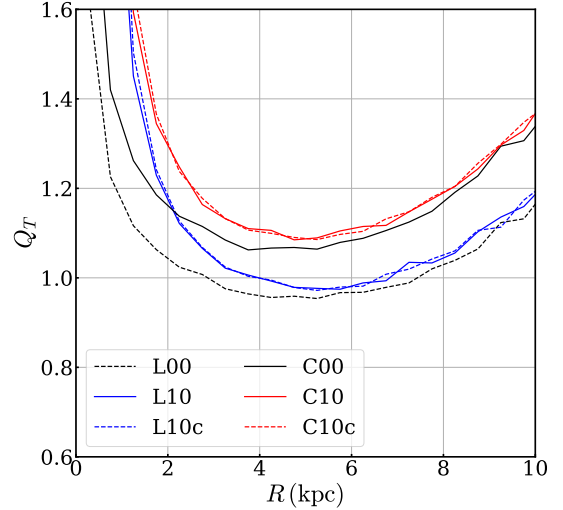


Figure 2. Radial profiles of Q_T for models with $M_b/M_d = 0, 0.1$. The minimum value $Q_{T,\text{min}}$ occurs at $R \sim 4\text{--}6 \text{ kpc}$, which tends to be larger for a galaxy with a more concentrated halo and/or more massive bulge.

The gravitational susceptibility of a disk can be measured by the Toomre (1966) stability parameter

$$Q_T = \frac{\kappa \sigma_R}{3.36 G \Sigma_d}, \quad (7)$$

where κ is the epicycle frequency and Σ_d is the disk surface density. Figure 2 plots the radial distributions of Q_T for models with $M_b/M_d = 0$ and 0.1 . Overall, Q_T is large at both small R (due to increase in κ) and large R (due to decrease in Σ_d) and attains a minimum value $Q_{T,\text{min}}$ at $R \sim 4\text{--}6 \text{ kpc}$. Our galaxy models have $Q_{T,\text{min}}$ in the range between 0.95 and 1.16 (Table 1): $Q_{T,\text{min}}$ tends to be larger for a galaxy with a centrally concentrated halo and/or more massive bulge, while it is almost independent of the bulge compactness.

2.2. Numerical Method

To construct the initial galaxy models, we make use of the GALIC code (Yurin & Springel 2014) which solves the collisionless Boltzmann equations to find a desired equilibrium state by optimizing the velocities of individual particles. We distribute $N_d = 1.0 \times 10^6$, and $N_b = 5 \times 10^4\text{--}5 \times 10^5$, and $N_h = 2.6 \times 10^7$ particles for the disk, bulge, and halo, respectively. We set the mass of each particle to $m = 5 \times 10^4 M_\odot$, which are equal for all three components.

We evolve our galaxy models by using a public version of the Gadget-4 code (Springel et al. 2021). This version has improved force accuracy, time-stepping, computational efficiency, and parallel scalability from Gadget-3. It offers the Fast Multipole Method in which the tree is accelerated by multipole expansion not only at the

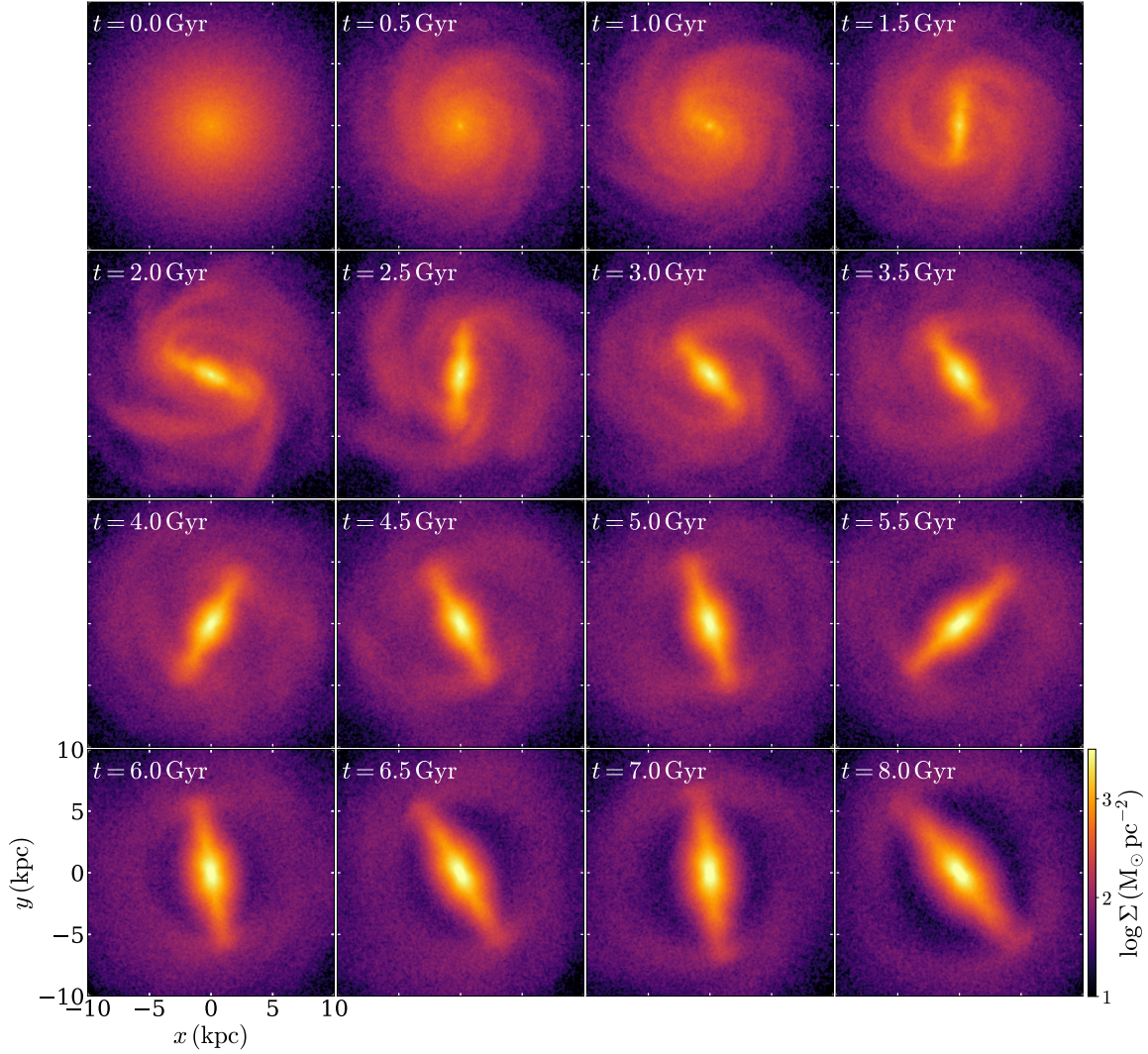


Figure 3. Snapshots of the disk surface density in model C10.

source side but also at the sink side. For our galaxy models, we find the multipole expansion to order $p = 4$ is fastest. In addition, hierarchical time-integration scheme can effectively reduce the computation time by constructing a tree only for the set of particles involved in the current force calculation. We take the force accuracy parameter $\alpha = 3 \times 10^{-4}$ which conserves the total angular momentum within ~ 0.1 percent (see below). The softening parameters for dark halo, stellar disk, and bulge particles are set to 0.05 kpc, 0.01 kpc, and 0.01 kpc, respectively.

3. RESULTS

In this section, we present evolution of our models with a focus on the temporal changes in the strength, pattern speed, and size of the bars that form. The bar formation conditions will be discussed in [Section 4](#).

3.1. Bar Formation and Strength

[Figure 3](#) plots snapshots of the disk surface density for our fiducial model C10. [Figure 4](#) plots the snapshots of all the models at $t = 8.0$ Gyr. In model C10 with $Q_{T,\min} = 1.09$, non-axisymmetric perturbations inherent in the particle distributions grow as they swing from leading to trailing configurations (e.g., [Binney & Tremaine 2008](#); [Kim & Ostriker 2007](#); [Kwak et al. 2017](#); [Seo et al. 2019](#)), forming spiral arms at $t = 0.5$ Gyr. Since the inner Lindblad resonance (ILR) is weak in this model, trailing spiral waves propagate toward the galaxy center to become leading waves at the opposite side, which can grow further: successive swing amplifications combined with multiple feedback loops eventually lead to a bar at $t \gtrsim 1.5$ Gyr. If $Q_{T,\min}$ is quite small, as in models C00 and L00, the swing amplification is so virulent that the inner parts of the spiral arms are rapidly organized into a bar in less than ~ 1 Gyr. In contrast,

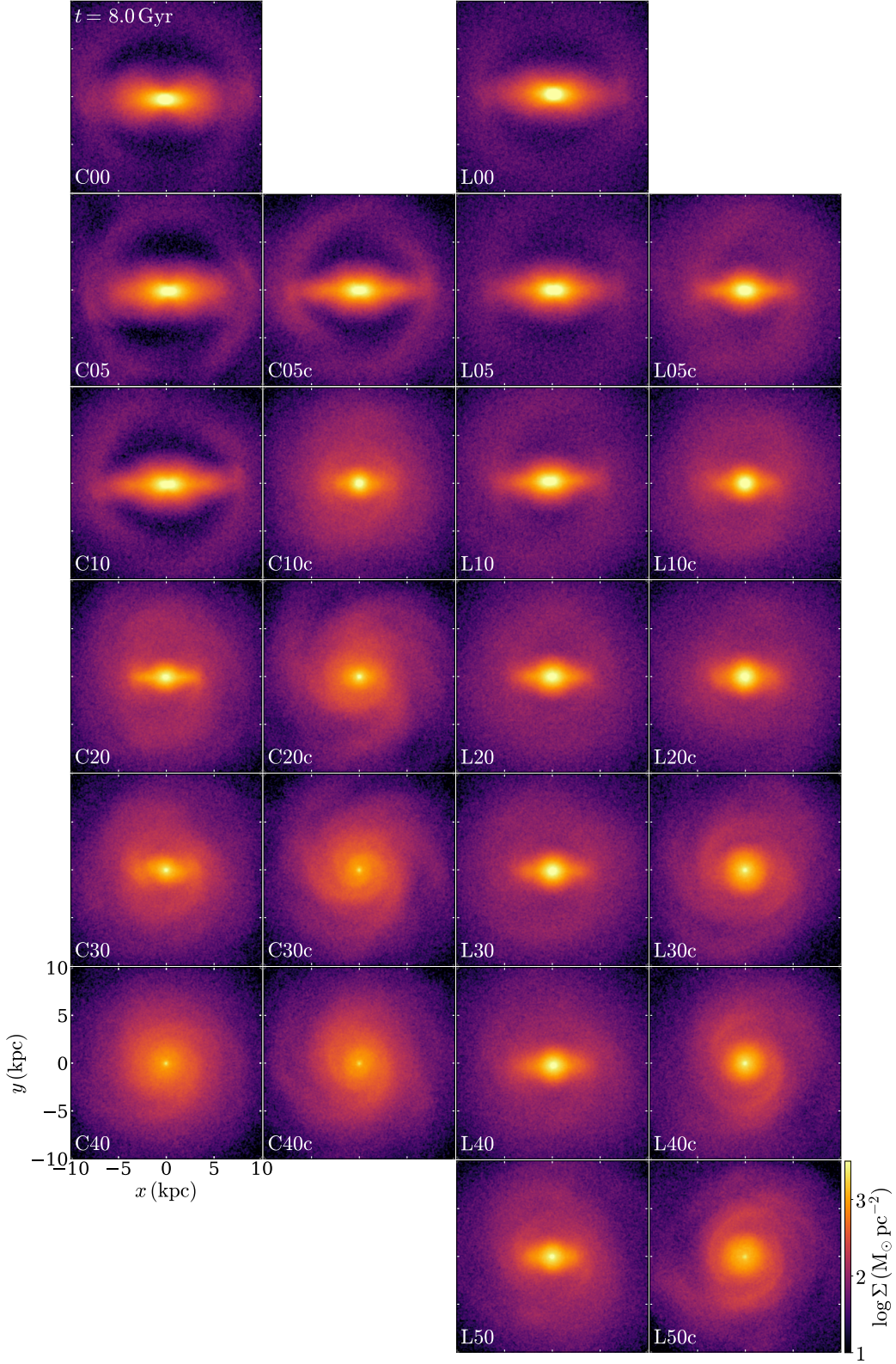


Figure 4. Snapshots of the disk surface density at $t = 8.0$ Gyr in all the models. Each image is rotated such that the semi-major axis of a bar (or an oval) is aligned parallel to the x -axis.

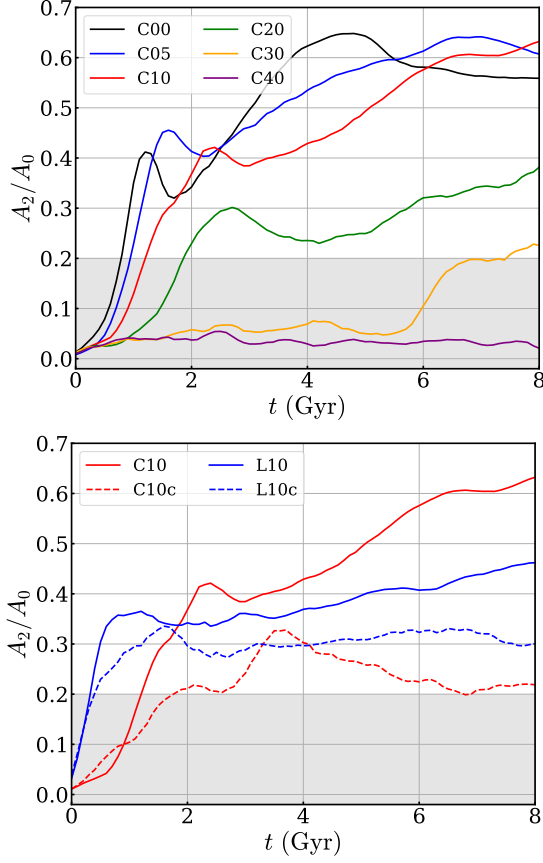


Figure 5. Temporal changes of the bar strength A_2/A_0 for models with less compact bulges in the C series (top) and for models with $M_b/M_d = 0.1$ (bottom). Features with $A_2/A_0 \leq 0.2$ are regarded as ovals or spirals.

if $Q_{T,\min}$ is large or the ILR is too strong, as in models C40, C20c, and L30c, the feedback loop is blocked and the disks produce only spirals, sometimes with an oval.

To quantify the bar strength, we first consider an annular region of the disk centered at radius R with width $\Delta R = 1$ kpc and calculate the amplitudes of the $m = 2$ Fourier modes as

$$a_2(R) = \sum_i m_i \cos(2\theta_i), \quad (8a)$$

$$b_2(R) = \sum_i m_i \sin(2\theta_i), \quad (8b)$$

where θ_i and m_i are the azimuthal angle and mass of the i -th disk particle in the annulus, respectively. We then define the bar strength as

$$\frac{A_2}{A_0} = \max \left(\frac{\sqrt{a_2^2 + b_2^2}}{\sum_i m_i} \right). \quad (9)$$

Note that A_2/A_0 measures the strength of $m = 2$ spirals when a bar is absent or weak. For spirals, the position

angle

$$\psi(R) \equiv \frac{1}{2} \tan^{-1} \left(\frac{b_2}{a_2} \right) \quad (10)$$

systematically varies with R , while $\psi(R)$ remains almost constant for a bar.

Following [Algorry et al. \(2017\)](#), we regard galaxies with $A_2/A_0 \geq 0.2$ and relatively constant $\psi(R)$ as being barred: features with $A_2/A_0 < 0.2$ are considered as ovals if $\psi(R)$ is constant or spirals if $\psi(R)$ changes with R . [Figure 5](#) plots temporal evolution of A_2/A_0 for models with less compact bulges in the C series (upper panel) and for models with $M_b/M_d = 0.1$ (lower panel). The evolution of A_2/A_0 is dominated by spirals at early time ($\lesssim 1-2$ Gyr) and then by a bar. Although the spirals are strong in the outer regions, they can affect the inner disk where a bar exists before it fully grows (see the $t \leq 3$ Gyr panels in [Figure 3](#)). The spirals and bar rotate about the galaxy center at different pattern speeds. When the spirals and bar become in phase, A_2/A_0 achieves its peak value temporarily (at $t = 2.3$ Gyr for model C10). Subsequently, A_2/A_0 decreases as they become out of phase, although it increases again as the bar grows further and dominates the inner disk. The presence of a more massive bulge makes the bar forms later and weaker. The bar formation is completely suppressed in models with $M_b/M_d \geq 0.4$ in the C series.

The compactness of halo and bulge has a significant effect on the bar formation. In the L series with a less concentrated halo, disks are unstable to form a bar even when the bulge mass amounts to $\sim 50\%$ of the disk mass. In contrast, disks in the C series with a compact halo do not produce a bar when $M_b/M_d \gtrsim 0.35$. Similarly, a more compact bulge tends to suppress the bar formation. For example, the maximum bulge mass for bar formation is decreased to 20% and 10% in the L and C series, respectively, when the bulge is compact. Our result that a bar does not form in galaxies with a very massive and compact bulge is qualitatively consistent with previous studies (e.g., [Kataria & Das 2018](#); [Saha & Elmegreen 2018](#)).

3.2. Buckling Instability

[Figure 6](#) plots the temporal changes in the ratio, σ_z/σ_R , of the vertical to radial velocity dispersion of the disk particles at $R = 1$ kpc for models with $M_b/M_d \leq 0.2$ in the C series together with model L00. Since a bar is supported by x_1 orbits elongated along the bar semi-major axis, its growth naturally involves the increase in σ_R . At the same time, the bar and spirals can excite the vertical motions of star particles, enhancing σ_z (e.g., [Quillen et al. 2014](#)). When a bar grows rapidly, as in models C00 and L00, σ_R increases faster than σ_z ,

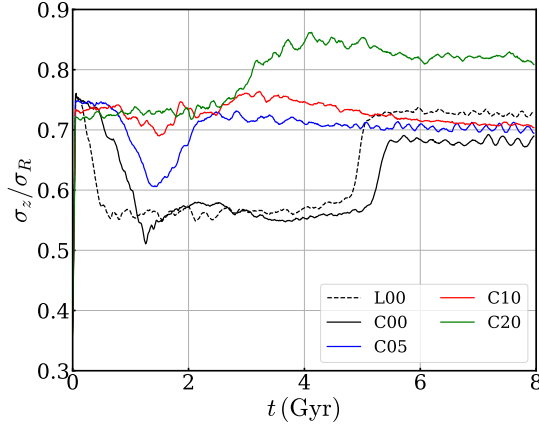


Figure 6. Time evolution of the ratio, σ_z/σ_R , of the velocity dispersions at $R = 1$ kpc for models with $M_b/M_d \leq 0.2$ in the C series together with model L00. A rapid increase of σ_z/σ_R at $t \sim 5$ Gyr in models C00 and L00 is due to buckling instability.

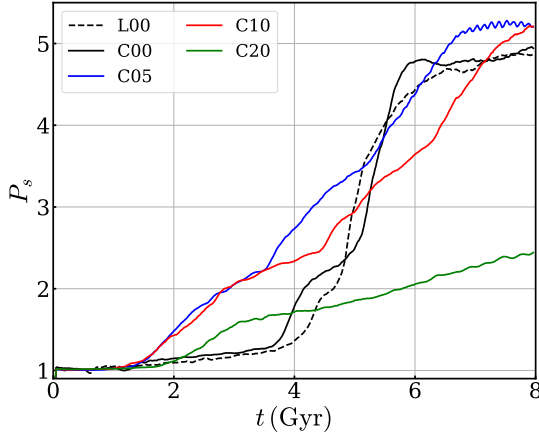


Figure 7. Time evolution of the B/P strength, P_s , defined in Equation (11), for models shown in Figure 6. In most models, P_s increases relatively slowly, while it increases rapidly at $t \sim 5$ Gyr in models C00 and L00, corresponding to buckling instability.

resulting in a decrease in the ratio σ_z/σ_R at early time. When a bar grows slowly, in contrast, σ_z/σ_R remains more or less constant.

The increase in σ_z leads to the disk thickening and the formation of a boxy/peanut (B/P) bulge. All the bars that form in our models evolve to B/P bulges. Figure 7 plots evolution of the B/P strength, defined as

$$P_s = \max \left(\frac{|\tilde{z}|}{|\tilde{z}_0|} \right), \quad (11)$$

where the tilde denotes the median and z_0 is the initial value (Iannuzzi & Athanassoula 2015; Fragkoudi et al. 2017; Seo et al. 2019), for models with $M_b/M_d \leq 0.2$.

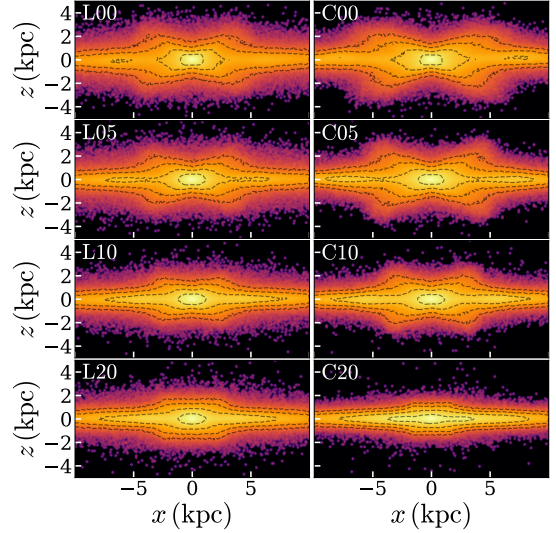


Figure 8. Contours of logarithm of the projected disk densities at $t = 6.0$ Gyr in models with $M_b/M_d \leq 0.2$. The x - and z -axes correspond to the bar semi-major axis and the vertical direction, respectively. The dotted contours denote $\Sigma = 10^{9.5}, 10^{9.0}, 10^{8.5}, 10^{8.0} \text{ M}_\odot \text{ kpc}^{-2}$ from inside to outside.

In most models, the disk thickening occurs secularly. However, P_s (as well as σ_z/σ_R) in models C00 and L00 increases rapidly at $t \sim 5$ Gyr, which is due to vertical buckling instability.

It is well known that a bar can undergo buckling instability when σ_z/σ_R is small. Toomre (1966) and Araki (1987) suggested that non-rotating thin disks are unstable to the buckling instability if $\sigma_z/\sigma_R \leq 0.3$. For realistic disks with spatially varying σ_z/σ_R , Raha et al. (1991) found that the buckling instability occurs if $\sigma_z/\sigma_R \lesssim 0.25\text{--}0.55$ in the mid-disk regions. By varying the values of σ_z/σ_R in N -body simulations, Martinez-Valpuesta et al. (2006) suggested that the critical value is at $\sigma_z/\sigma_R \sim 0.6$ (see also Kwak et al. 2017). This is consistent with our numerical results that models L00 and C00 have $\sigma_z/\sigma_R \lesssim 0.6$ before undergoing the buckling instability, as shown in Figure 6.

Figure 8 plots the edge-on views of the projected density distributions of the disks at $t = 6.0$ Gyr for models with $M_b/M_d \leq 0.2$. The x - and z -directions correspond to the direction parallel to the bar semi-major axis and the vertical direction, respectively. The density distributions in models L00 and C00 with no bulge are asymmetric with respect to the $z = 0$ plane, evidencing the operation of buckling instability (Martinez-Valpuesta et al. 2006). We note that the other models with a bulge also possess a B/P bulge which develops on a timescale longer than in models L00 and C00. This is consistent with Sellwood & Gerhard (2020) who showed that the presence

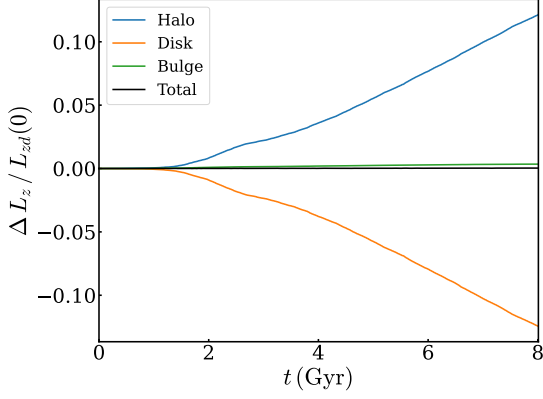


Figure 9. Temporal changes of the angular momentum of the disk (orange), halo (blue), bulge (green), and the total (black) for model C10. All angular momenta and their changes are relative to the initial angular momentum of the disk $L_{zd}(0)$.

of a nuclear mass with only a small ($\sim 2.5\%$) fraction of the disk mass tends to suppress the buckling instability. In models with a bulge, the disks appear to thicken as the bar particles are excited vertically by the passage through the 2 : 1 vertical resonance (Quillen et al. 2014; Sellwood & Gerhard 2020).

3.3. Angular Momentum and Pattern Speed

We calculate the angular momentum of each component as

$$L_z = \sum_i m_i (xv_y - yv_x). \quad (12)$$

Figure 9 plots temporal changes of L_z relative to the initial disk angular momentum for a disk (orange), halo (blue), bulge (green), as well as the total (black) in model C10. The disk loses its angular momentum right after the bar formation, while the halo and bulge absorb it. Since the bulge occupies relatively a small volume in space in model C10, the amount of angular momentum it gains is limited to $\sim 4\%$, while the halo absorbs the remaining $\sim 96\%$. In model L50 with a large bulge mass, however, the bulge absorbs about $\sim 26\%$ of the angular momentum lost by the disk. The total angular momentum is conserved within $\sim 0.1\%$ in all models.

To calculate the bar pattern speed Ω_b , we use two methods: (1) the cross-correlation of the disk surface density in the annular regions with width $\Delta R = 0.1$ kpc at $R = 2$ kpc where most bars attain their maximum strength and (2) the temporal rate of changes in the position angle ψ , i.e., $\Omega_b = d\psi/dt|_{R=2 \text{ kpc}}$. We check that the two methods yield the pattern speeds that agree within $\sim 1\%$. Figure 10 plots evolution of the bar pattern speeds for selected models. The initial bar pattern speed depends on the bulge mass in such a way that a

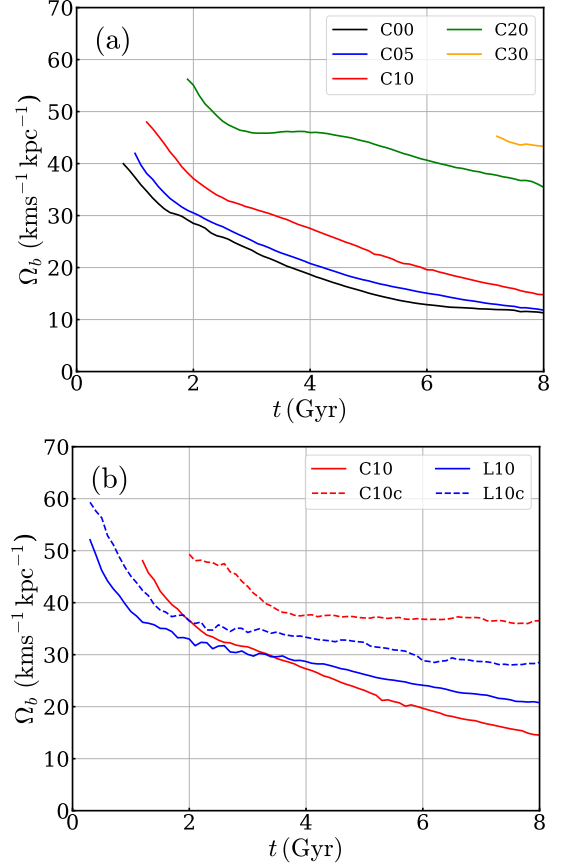


Figure 10. Temporal changes of the bar pattern speed Ω_b for the bar-forming models shown in Figure 5. In all models, Ω_b decreases over time due to angular momentum transfer from a bar to both halo and bulge.

more massive bulge tends to have larger Ω_b (Kataria & Das 2018, 2019). In all models, a bar becomes slower over time due to the transfer of angular momentum to both halo and bulge.

Figure 11 plots the temporal changes in the bar slow-down rate, $-d\Omega_b/dt$, for the models shown in Figure 10(a), showing that there is no systematic dependence between the bar slow-down rate and the bulge mass. This result is different from Kataria & Das (2019) who found that the rate is higher for a more massive bulge. The discrepancy may be due to the differences in the bulge (and halo) compactness. The models considered by Kataria & Das (2019) have $R_b/R_d \leq 0.18$ with R_b being the half-mass bulge radius, which is more compact than our models in the C series that have $R_b/R_d = (1 + \sqrt{2})a_b/R_d = 0.32$. Figure 12 of Kataria & Das (2018) shows no systematic trend between the bar slow-down rate and the bulge mass for models with $0.43 < R_b/R_d < 0.47$. This suggests the bulge should be sufficiently compact to control the temporal evolution of the bar pattern speed. In our models with less

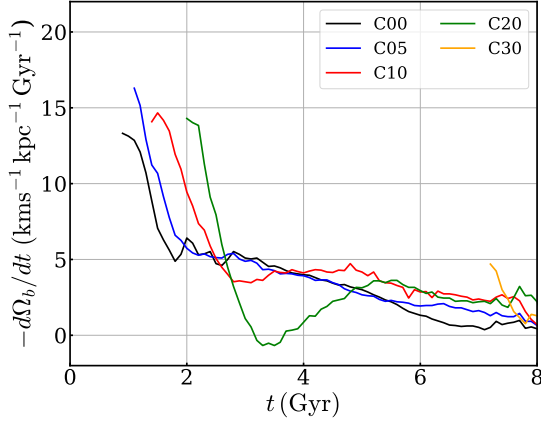


Figure 11. Temporal variations of the slow-down rate of the bar pattern speed for the models shown in Figure 10(a).

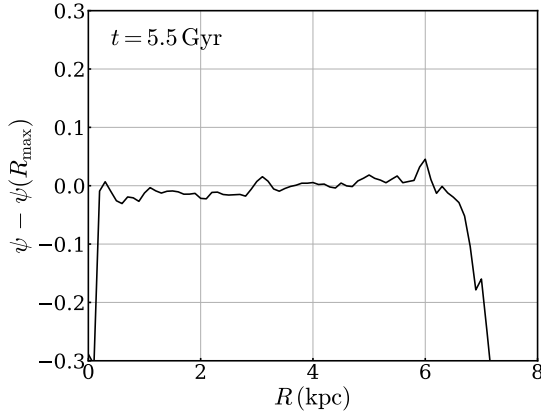


Figure 12. Radial distribution of $\psi - \psi(R_{\max})$ of the $m = 2$ mode in the disk of model C10 at $t = 5.5$ Gyr. Here, R_{\max} denotes the radius where A_2/A_0 is maximized. The bar has a length $R_b = 6.8$ kpc at this time.

compact bulge than in Kataria & Das (2019), angular momentum is predominantly absorbed by the halo (see Figure 9).

3.4. Bar Length

One can use the position angle $\psi(R)$ defined in Equation (10) to measure the bar length (e.g., Athanassoula & Misiriotis 2002; Scannapieco & Athanassoula 2012). Figure 12 plots the radial distribution of the position angle of the $m = 2$ mode in the disk of model C10 at $t = 5.5$ Gyr. Note that $\psi(R)$ that remains more or less constant at small R changes abruptly at $R \gtrsim 6.8$ kpc, indicating that the bar has a semi-major axis $R_b = 6.8$ kpc at this time.

Figure 13 plots temporal changes of R_b for the models shown in Figure 10. First of all, bars are longer in models with a less massive and/or less compact bulge

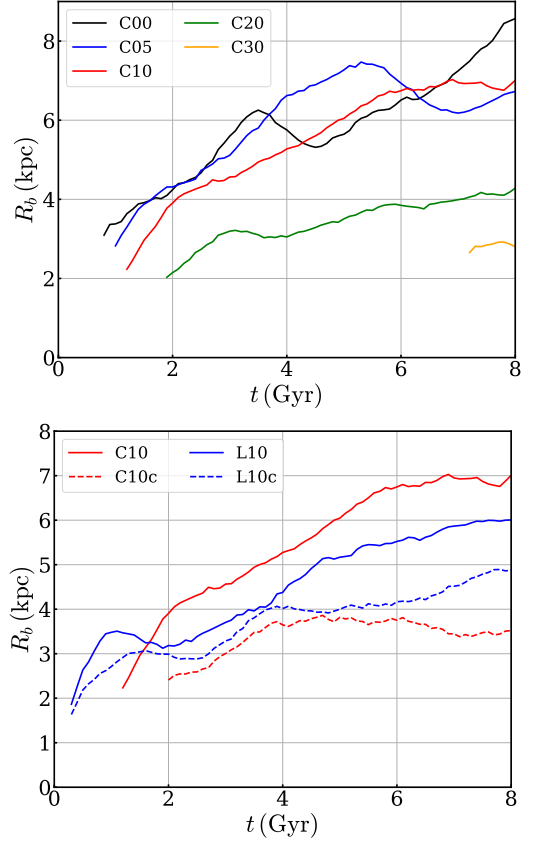


Figure 13. Temporal changes of the bar length R_b for the models shown in Figure 10.

since these allow stronger swing amplifications. Overall, the bar length in our models increases with time, expedited by angular momentum exchange with the halo and bulge (Athanassoula 2003). The increasing rate of the bar length is lower in models with more massive and compact bulge. We note that the decrease of the bar length at $t \sim 3.8$ Gyr in model C00, $t \sim 5.3$ Gyr in model C05, and $t \sim 3.3$ Gyr C20 is caused by the interactions with surrounding spiral arms (or an inner ring) which tend to shorten the bar by perturbing particles on outer x_1 orbits. In model L10, outer spiral arms are in phase with the bar at $t \sim 1$ Gyr, making R_b longer than the true bar length temporarily.

Figure 14 plots the dependence of the bar pattern speed Ω_b and the corotation radius R_{CR} on the bar length R_b in all models that form a bar, with the symbol size representing the simulation time. In general, longer bars tend to be slower. The ratio $\mathcal{R} = R_{\text{CR}}/R_b$ is useful to classify slow or fast bars: bars with $\mathcal{R} > 1.4$ are considered slow, while those with $\mathcal{R} < 1.4$ are termed fast bars. Models with a massive and compact bulge have larger \mathcal{R} since they have short bars compared to those

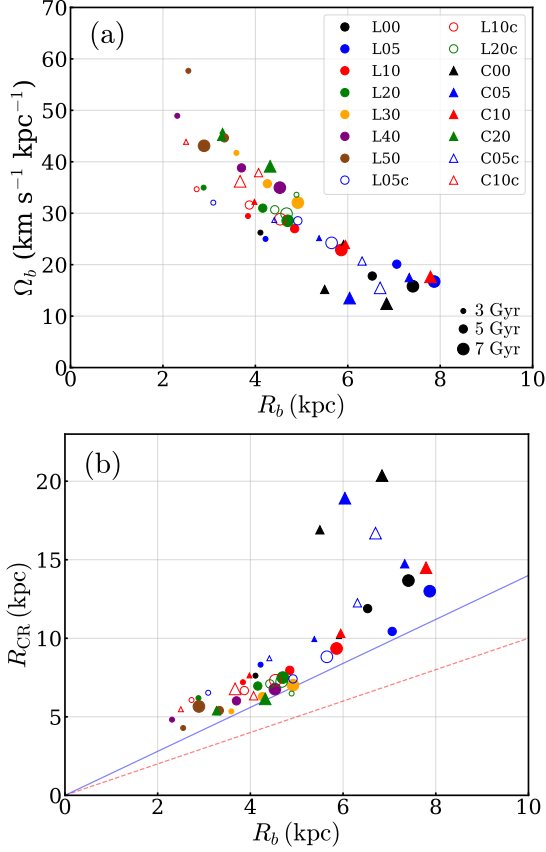


Figure 14. Relationship (a) between Ω_b and R_b and (b) between R_{CR} and R_b for all models that form a bar. The marker sizes correspond to the simulation times. The red dashed and blue solid lines in (b) draw $\mathcal{R} \equiv R_{CR}/R_b = 1.0$ and 1.4, respectively, indicating that all bars in our models are slow with $\mathcal{R} > 1.4$.

with a less compact bulge. Note that all bars are slow rotators for almost all time.

4. DISCUSSION

In the preceding section, we have shown that models with a massive and compact bulge and a concentrated halo are less likely to form a bar. In this section we compare our numerical results with the previous bar formation conditions mentioned in Section 1. We then propose a new two-parameter condition that is consistent with the theory of bar formation. We also use our numerical results to indirectly measure the mass of the classical bulge in the Milky Way.

4.1. Criteria for Bar Formation

Figure 15 plots the simulation outcomes in the t_{OP} - ϵ_{ELN} plane, with the blue and red symbols representing unstable and stable models to bar formation, respectively: the values of t_{OP} and ϵ_{ELN} of each model are listed in Columns (7) and (8) of Table 1. Circles and

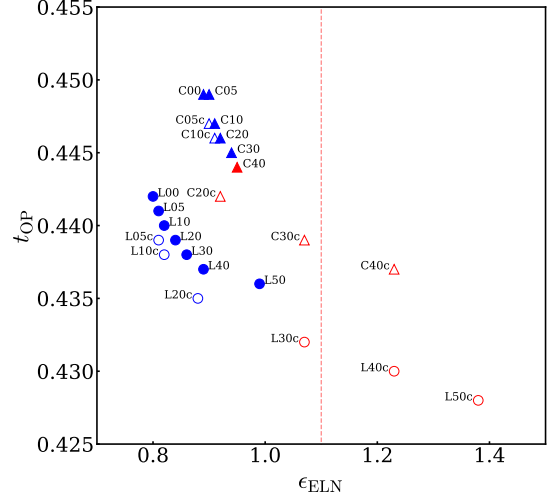


Figure 15. Simulation outcomes in the t_{OP} - ϵ_{ELN} plane. The vertical dashed line marks $\epsilon_{ELN} = 1.1$ (Equation 2). Blue symbols denote unstable models for bar formation, while red symbols are for stable models. Circles and triangles are for models in the L and C series, respectively. Open and filled symbols correspond to models with compact and less compact bulges, respectively.

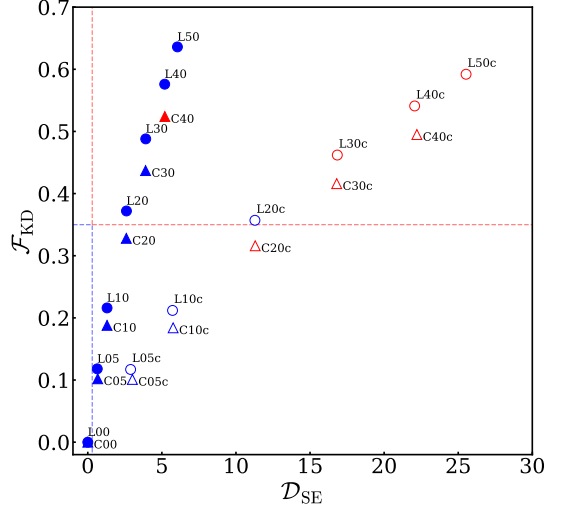


Figure 16. Same as Figure 15 but in the \mathcal{F}_{KD} - \mathcal{D}_{SE} plane. The horizontal and vertical dashed lines draw $\mathcal{F}_{KD} = 0.35$ and $\mathcal{D}_{SE} = 1/\sqrt{10}$ (see Equations (3) and (4)), respectively.

triangles mark the models in the L and C series, respectively, with the open (filled) symbols corresponding to the compact (less compact) bulges. While all the models have $t_{OP} > 0.42$, some of them do not evolve to form a bar, suggesting that t_{OP} is not a good indicator of the disk stability against bar formation. This is most likely because Ostriker & Peebles (1973) employed models with a fixed halo, neglecting halo-disk interactions

which are crucial for the bar growth. Saha & Elmegreen (2018) also noted that the initial value of t_{OP} cannot determine whether a bar forms or not.

The abscissa of Figure 15 shows that all the bar-forming models satisfy the ELN criterion (Equation 2). However, some galaxies with a massive bulge under a concentrated halo remain stable even with $\epsilon_{\text{ELN}} < 1.1$. The discrepancy between the ELN criterion and our results is because it, based on 2D thin-disk models with a fixed halo, does not capture the disk-halo interactions (e.g., Athanassoula 2008; Fujii et al. 2018). Analyses of galaxies in recent simulations for cosmological galaxy formation such as EAGLE and IllustrisTNG, etc. have also found that ϵ_{ELN} is incomplete to predict whether galaxies formed are barred or not (Yurin & Springel 2015; Algorry et al. 2017; Marioni et al. 2022; Izquierdo-Villalba et al. 2022).

Figure 16 plots our results in the $\mathcal{F}_{\text{KD}}-\mathcal{D}_{\text{SE}}$ plane, with the blue and red symbols corresponding to the unstable and stable models, respectively: the values of \mathcal{F}_{KD} and \mathcal{D}_{SE} of each model are given in Columns (9) and (10) of Table 1. The ordinate of Figure 16 shows that Equation (3) is overall consistent with the simulation results for the models in the C series, although it fails for the models in the L series: some models with a massive bulge under a less concentrated halo form a bar even with $\mathcal{F}_{\text{KD}} > 0.35$. In fact, all the models in Kataria & Das (2018) belong to our C series, so that their criterion is unable to predict bar formation in models with less concentrated halos.¹

Saha & Elmegreen (2018) found that a compact bulge suppresses feedback loops by making the ILR strong. According to Equation (4) for bar formation, all of our models except models C00 and L00 with no bulge should not form a bar. However, the abscissa of Figure 16 shows that most models with $\mathcal{D}_{\text{SE}} \lesssim (4-10)$ are unstable to bar formation. It is unclear why our results are so different from Equation (4), but the parts of the reason may be that compared with our models, their halos are small in mass with $M_h \sim 4M_d$ and their disks are thin with $z_d \sim 0.02R_d$.

As mentioned earlier, bar formation in a disk involves several cycles of swing amplifications and feedback loops. This naturally requires two conditions: (1) the disk should have small $Q_{T,\text{min}}$ to be sufficiently susceptible to self-gravitational instability and (2) the ILR should be weak enough for incoming waves pass

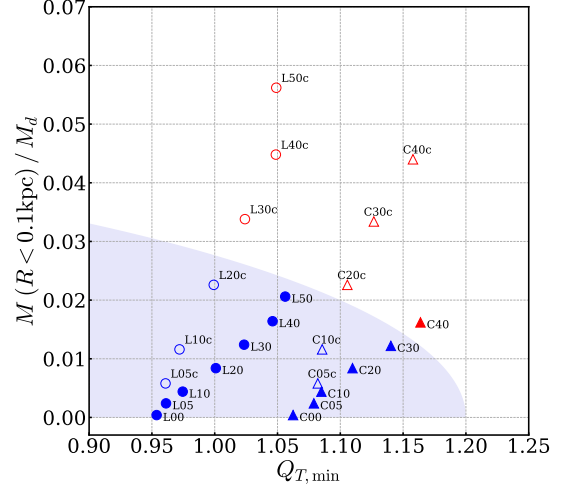


Figure 17. Same as Figure 16 but in the $Q_{T,\text{min}}-\text{CMC}$ plane. The shaded regions correspond to Equation 13, within which all the bar-forming models are located.

through the center, which is achieved when the CMC is small. Motivated by these physical considerations, Figure 17 plots the simulation outcomes in the $Q_{T,\text{min}}-\text{CMC}$ plane. Models with more compact bulge and halo have a higher CMC than the less concentrated counterparts with the same M_b/M_d . Models with concentrated halos tend to have higher $Q_{T,\text{min}}$, although $Q_{T,\text{min}}$ is insensitive to the bulge compactness. Note that all the bar-forming models satisfy

$$\left(\frac{Q_{T,\text{min}}}{1.2}\right)^2 + \left(\frac{\text{CMC}}{0.05}\right)^2 < 1, \quad (13)$$

marked as a shade in Figure 17. In models with $Q_{T,\text{min}}$ or CMC larger than Equation 13 implies, swing amplifications with suppressed feedback loops are not strong enough to promote bar formation: these models end up with only weak spiral arms in outer disks (see Figure 4).

Failure of Equations (3) and (4) as a criterion for bar formation is because they account only for a bulge in setting the ILR. However, our results show that not only the bulge mass but also the halo mass in the galaxy center are important in determining the strength of the ILR.

4.2. Fast or Slow Bars

The fact that all bars in our models are slow is consistent with the results of Roshan et al. (2021) who found that bars formed in cosmological hydrodynamical simulations are preferentially slow, with the mean value of $\mathcal{R} \sim 1.9-3.0$. However, Cuomo et al. (2020) showed that most observed bars in 77 nearby galaxies are fast, with a mean value of $\mathcal{R} \sim 0.92$. What causes the discrepancy in the bar properties between observations and simulations

¹ The halos employed in Kataria & Das (2018) have the scale radius of $a_h = 17.88$ kpc for the MA models and $a_h = 25.54$ kpc for the MB models (S. K. Kataria, 2022, private communication), which are smaller than $a_h = 30$ kpc for the models in our C series.

is a challenging question. Frankel et al. (2022) argued that the discrepancy arises not because the simulated bars are too slow but because they are too short.

There is a large room for improvement in both simulations and observations for more reliable comparisons. In simulations, our isolated-galaxy models need to be more realistic by including a gaseous component, star formation, halo spin, etc., which may affect the bar pattern speeds significantly. Cosmological simulations still suffer from issues such as insufficient resolution and calibration of feedback from star formation and active galactic nuclei. In observations, the often-used Tremaine-Weinberg method in measuring the bar pattern speeds depends critically on the assumptions that galaxies are in a steady state and that there is a well-defined pattern (Tremaine & Weinberg 1984), the validity of which is not always guaranteed. In addition, the bar length depends considerably on the measurement methods such as Fourier analysis, force ratio, ellipse fitting, etc. (Lee et al. 2022). Theoretically, it is impossible to have a long-lived, quasi-steady bar with $\mathcal{R} < 1$ since the bar-supporting x_1 orbits exist only inside the corotation radius (e.g., Contopoulos 1980; Contopoulos & Grosbøl 1989; Binney & Tremaine 2008).

4.3. Classical Bulge of the Milky Way

The Milky Way is a barred galaxy dominated by a B/P bulge (e.g., Dwek et al. 1995; Martinez-Valpuesta & Gerhard 2011; Ness et al. 2013). Some early studies reported that the bar in the Milky Way is fast and short, with $50 < \Omega_b < 60 \text{ km s}^{-1} \text{ kpc}^{-1}$ and $R_b \sim 3 \text{ kpc}$ (Fux 1999; Debattista et al. 2002; Bissantz et al. 2003; Fragkoudi et al. 2019; Dehnen 2000), while recent studies suggested that it is rather slow and long, with $33 < \Omega_b < 45 \text{ km s}^{-1} \text{ kpc}^{-1}$ and $R_b \sim 4.5\text{--}5 \text{ kpc}$ (Wegg et al. 2015; Sormani et al. 2015; Portail et al. 2017; Bland-Hawthorn & Gerhard 2016; Clarke & Gerhard 2022). By comparing observed proper motions in the bar and bulge regions with dynamical models, Clarke & Gerhard (2022) most recently reported $\Omega_b = 33.29 \pm 1.81 \text{ km s}^{-1} \text{ kpc}^{-1}$, placing the corotation resonance at $R_{\text{CR}} \sim 5\text{--}7 \text{ kpc}$.

Using our numerical results, we attempt to constrain the mass of the classical bulge of the Milky Way. As Figures 10 and 13 show, the bar in model C10 has $\Omega_b \sim 30\text{--}35 \text{ km s}^{-1} \text{ kpc}^{-1}$ and $R_b \sim 4.5\text{--}5 \text{ kpc}$ at $t = 2.5\text{--}3.5 \text{ Gyr}$, which are well matched to the observed properties of the Milky-Way bar. Model C20 produces a bar with $\Omega_b \sim 36 \text{ km s}^{-1} \text{ kpc}^{-1}$ and $R_b \sim 4.2 \text{ kpc}$ at $t = 8 \text{ Gyr}$. The bars in models C00 and C05 have a length of $R_b \sim 5 \text{ kpc}$ at $t \sim 2.5 \text{ Gyr}$, but their pattern speeds are smaller than $30 \text{ km s}^{-1} \text{ kpc}^{-1}$. These results suggest that the Milky may possess a classical bulge with mass

$\sim 10\text{--}20\%$ of the disk mass. This is consistent with the claim of Shen et al. (2010) that the classical bulge of the Milky Way should be less than 25% of the disk mass to be fitted well with the observed stellar kinematics (see also Di Matteo et al. 2015). If the age of the Milky-Way bar is $\sim 3 \text{ Gyr}$, as proposed by Cole & Weinberg (2002) based on the ages of infrared carbon stars, the bar in model C10 best represents the Milky Way bar. If it is instead $\sim 8 \text{ Gyr}$ old, as proposed by Bovy et al. (2019) based on the kinematic analyses of APOGEE and *Gaia* data, it would be better described by the bar in model C20.

5. CONCLUSIONS

We have presented the results of N -body simulations to study the effects of spherical components including a classical bulge and a dark halo on the formation and evolution of a bar. For this, we have constructed 3D galaxy models with physical conditions similar to the Milky Way and varied the bulge-to-disk mass ratio as well as the compactness of the halo and bulge components, while fixing the disk and halo masses. Our main conclusions are highlighted below.

1. *Bar Properties* – The presence of a massive bulge delays the bar formation. A bar forms later and weaker in models with a more massive and compact bulge and under a more concentrated halo. Bars are shorter and thus rotate faster in models with more massive and compact bulges. Angular momentum transfer from a bar to both halo and bulge makes the bar slower and longer over time, although most of the angular momentum lost by the bar is absorbed by the halo. All the bars in our models are slow rotators with $\mathcal{R} = R_{\text{CR}}/R_b > 1.4$.
2. *B/P Bulge and Buckling Instability* – All the models that form a bar undergo disk thickening and eventually develop a B/P bulge. In all models with a bulge, this proceeds secularly as the bulge tends to suppress the bar formation. However, two models (L00 and C00) with no bulge experience buckling instability at $t \sim 5 \text{ Gyr}$ during which the bar thickens rapidly. The buckling instability occurs when σ_z/σ_R is kept below ~ 0.6 and involves asymmetric density distribution of the disk across the $z = 0$ plane.
3. *Conditions for Bar Formation* – Our numerical results for bar formation are not well explained by the single-parameter criteria proposed by the previous studies. We instead find that the bar formation in our galaxy models need to satisfy Equation (13). In models with larger $Q_{T,\text{min}}$ or larger

CMC, the growth of perturbations via swing amplifications combined with feedback loops is too weak to produce bar-supporting x_1 orbits.

4. *Classical Bulge of the Milky Way* – Among our models, the bar at $t \sim 2.5\text{--}3.5$ Gyr in model C10 or at $t \sim 8$ Gyr in model C20 is matched well with the observed ranges of the bar length and pattern speed in the Milky Way. This suggests that the Milky Way is most likely to possess a classical bulge with mass $\sim 10\text{--}20\%$ of the disk mass.

ACKNOWLEDGMENTS

We are grateful to the referee, Dr. Sandeep Kumar Katari, for an insightful report. This work was supported by the grants of National Research Foundation of Korea (2020R1A4A2002885 and 2022R1A2C1004810). Computational resources for this project were provided by the Supercomputing Center/Korea Institute of Science and Technology Information with supercomputing resources including technical support (KSC-2022-CRE-0017).

REFERENCES

- Aguerri, J. A. L., Méndez-Abreu, J., & Corsini, E. M. 2009, *A&A*, 495, 491, doi: [10.1051/0004-6361:200810931](https://doi.org/10.1051/0004-6361:200810931)
- Algorry, D. G., Navarro, J. F., Abadi, M. G., et al. 2017, *MNRAS*, 469, 1054, doi: [10.1093/mnras/stx1008](https://doi.org/10.1093/mnras/stx1008)
- Araki, S. 1987, *AJ*, 94, 99, doi: [10.1086/114451](https://doi.org/10.1086/114451)
- Athanassoula, E. 1992, *MNRAS*, 259, 345, doi: [10.1093/mnras/259.2.345](https://doi.org/10.1093/mnras/259.2.345)
- . 2002, *ApJL*, 569, L83, doi: [10.1086/340784](https://doi.org/10.1086/340784)
- . 2003, *MNRAS*, 341, 1179, doi: [10.1046/j.1365-8711.2003.06473.x](https://doi.org/10.1046/j.1365-8711.2003.06473.x)
- . 2008, *MNRAS*, 390, L69, doi: [10.1111/j.1745-3933.2008.00541.x](https://doi.org/10.1111/j.1745-3933.2008.00541.x)
- Athanassoula, E., Machado, R. E. G., & Rodionov, S. A. 2013, *MNRAS*, 429, 1949, doi: [10.1093/mnras/sts452](https://doi.org/10.1093/mnras/sts452)
- Athanassoula, E., & Misiriotis, A. 2002, *MNRAS*, 330, 35, doi: [10.1046/j.1365-8711.2002.05028.x](https://doi.org/10.1046/j.1365-8711.2002.05028.x)
- Baugh, C. M., Cole, S., & Frenk, C. S. 1996, *MNRAS*, 283, 1361, doi: [10.1093/mnras/283.4.1361](https://doi.org/10.1093/mnras/283.4.1361)
- Binney, J., & Tremaine, S. 2008, *Galactic Dynamics: Second Edition*
- Bissantz, N., Englmaier, P., & Gerhard, O. 2003, *MNRAS*, 340, 949, doi: [10.1046/j.1365-8711.2003.06358.x](https://doi.org/10.1046/j.1365-8711.2003.06358.x)
- Bland-Hawthorn, J., & Gerhard, O. 2016, *ARA&A*, 54, 529, doi: [10.1146/annurev-astro-081915-023441](https://doi.org/10.1146/annurev-astro-081915-023441)
- Bournaud, F., Combes, F., & Semelin, B. 2005, *MNRAS*, 364, L18, doi: [10.1111/j.1745-3933.2005.00096.x](https://doi.org/10.1111/j.1745-3933.2005.00096.x)
- Bournaud, F., Jog, C. J., & Combes, F. 2007, *A&A*, 476, 1179, doi: [10.1051/0004-6361:20078010](https://doi.org/10.1051/0004-6361:20078010)
- Bovy, J., Leung, H. W., Hunt, J. A. S., et al. 2019, *MNRAS*, 490, 4740, doi: [10.1093/mnras/stz2891](https://doi.org/10.1093/mnras/stz2891)
- Buta, R., & Combes, F. 1996, *FCPh*, 17, 95
- Buta, R. J., Sheth, K., Athanassoula, E., et al. 2015, *ApJS*, 217, 32, doi: [10.1088/0067-0049/217/2/32](https://doi.org/10.1088/0067-0049/217/2/32)
- Clarke, J. P., & Gerhard, O. 2022, *MNRAS*, 512, 2171, doi: [10.1093/mnras/stac603](https://doi.org/10.1093/mnras/stac603)
- Cole, A. A., & Weinberg, M. D. 2002, *ApJL*, 574, L43, doi: [10.1086/342278](https://doi.org/10.1086/342278)
- Collier, A., Shlosman, I., & Heller, C. 2018, *MNRAS*, 476, 1331, doi: [10.1093/mnras/sty270](https://doi.org/10.1093/mnras/sty270)
- . 2019, *MNRAS*, 489, 3102, doi: [10.1093/mnras/stz2327](https://doi.org/10.1093/mnras/stz2327)
- Contopoulos, G. 1980, *A&A*, 81, 198
- Contopoulos, G., & Grosbøl, P. 1989, *A&A Rv*, 1, 261, doi: [10.1007/BF00873080](https://doi.org/10.1007/BF00873080)
- Cuomo, V., Aguerri, J. A. L., Corsini, E. M., & Debattista, V. P. 2020, *A&A*, 641, A111, doi: [10.1051/0004-6361/202037945](https://doi.org/10.1051/0004-6361/202037945)
- de Vaucouleurs, G. 1963, *ApJ*, 138, 934, doi: [10.1086/147696](https://doi.org/10.1086/147696)
- Debattista, V. P., Gerhard, O., & Sevenster, M. N. 2002, *MNRAS*, 334, 355, doi: [10.1046/j.1365-8711.2002.05500.x](https://doi.org/10.1046/j.1365-8711.2002.05500.x)
- Debattista, V. P., & Sellwood, J. A. 2000, *ApJ*, 543, 704, doi: [10.1086/317148](https://doi.org/10.1086/317148)
- Dehnen, W. 2000, *AJ*, 119, 800, doi: [10.1086/301226](https://doi.org/10.1086/301226)
- Di Matteo, P., Gómez, A., Haywood, M., et al. 2015, *A&A*, 577, A1, doi: [10.1051/0004-6361/201424457](https://doi.org/10.1051/0004-6361/201424457)
- Díaz-García, S., Salo, H., Knapen, J. H., & Herrera-Endoqui, M. 2019, *A&A*, 631, A94, doi: [10.1051/0004-6361/201936000](https://doi.org/10.1051/0004-6361/201936000)
- Díaz-García, S., Salo, H., Laurikainen, E., & Herrera-Endoqui, M. 2016, *A&A*, 587, A160, doi: [10.1051/0004-6361/201526161](https://doi.org/10.1051/0004-6361/201526161)
- Dwek, E., Arendt, R. G., Hauser, M. G., et al. 1995, *ApJ*, 445, 716, doi: [10.1086/175734](https://doi.org/10.1086/175734)
- Efstathiou, G., Lake, G., & Negroponte, J. 1982, *MNRAS*, 199, 1069, doi: [10.1093/mnras/199.4.1069](https://doi.org/10.1093/mnras/199.4.1069)
- Fragkoudi, F., Di Matteo, P., Haywood, M., et al. 2017, *A&A*, 606, A47, doi: [10.1051/0004-6361/201630244](https://doi.org/10.1051/0004-6361/201630244)
- Fragkoudi, F., Katz, D., Trick, W., et al. 2019, *MNRAS*, 488, 3324, doi: [10.1093/mnras/stz1875](https://doi.org/10.1093/mnras/stz1875)

- Frankel, N., Pillepich, A., Rix, H.-W., et al. 2022, arXiv e-prints, arXiv:2201.08406.
<https://arxiv.org/abs/2201.08406>
- Fujii, M. S., Bédorf, J., Baba, J., & Portegies Zwart, S. 2018, *MNRAS*, 477, 1451, doi: [10.1093/mnras/sty711](https://doi.org/10.1093/mnras/sty711)
- Fux, R. 1999, *A&A*, 345, 787.
<https://arxiv.org/abs/astro-ph/9903154>
- Guiglion, G., Recio-Blanco, A., de Laverny, P., et al. 2015, *A&A*, 583, A91, doi: [10.1051/0004-6361/201525883](https://doi.org/10.1051/0004-6361/201525883)
- Hasan, H., Pfenniger, D., & Norman, C. 1993, *ApJ*, 409, 91, doi: [10.1086/172644](https://doi.org/10.1086/172644)
- Helmi, A. 2020, *ARA&A*, 58, 205,
doi: [10.1146/annurev-astro-032620-021917](https://doi.org/10.1146/annurev-astro-032620-021917)
- Hernquist, L. 1990, *ApJ*, 356, 359, doi: [10.1086/168845](https://doi.org/10.1086/168845)
- Hohl, F. 1976, *AJ*, 81, 30, doi: [10.1086/111849](https://doi.org/10.1086/111849)
- Holley-Bockelmann, K., Weinberg, M., & Katz, N. 2005, *MNRAS*, 363, 991, doi: [10.1111/j.1365-2966.2005.09501.x](https://doi.org/10.1111/j.1365-2966.2005.09501.x)
- Hopkins, P. F., Somerville, R. S., Cox, T. J., et al. 2009, *MNRAS*, 397, 802, doi: [10.1111/j.1365-2966.2009.14983.x](https://doi.org/10.1111/j.1365-2966.2009.14983.x)
- Hopkins, P. F., Bundy, K., Croton, D., et al. 2010, *ApJ*, 715, 202, doi: [10.1088/0004-637X/715/1/202](https://doi.org/10.1088/0004-637X/715/1/202)
- Iannuzzi, F., & Athanassoula, E. 2015, *MNRAS*, 450, 2514, doi: [10.1093/mnras/stv764](https://doi.org/10.1093/mnras/stv764)
- Izquierdo-Villalba, D., Bonoli, S., Rosas-Guevara, Y., et al. 2022, *MNRAS*, 514, 1006, doi: [10.1093/mnras/stac1413](https://doi.org/10.1093/mnras/stac1413)
- Kataria, S. K., & Das, M. 2018, *MNRAS*, 475, 1653, doi: [10.1093/mnras/stx3279](https://doi.org/10.1093/mnras/stx3279)
- . 2019, *ApJ*, 886, 43, doi: [10.3847/1538-4357/ab48f7](https://doi.org/10.3847/1538-4357/ab48f7)
- Kataria, S. K., Das, M., & Barway, S. 2020, *A&A*, 640, A14, doi: [10.1051/0004-6361/202037527](https://doi.org/10.1051/0004-6361/202037527)
- Kataria, S. K., & Shen, J. 2022, arXiv e-prints, arXiv:2210.14526. <https://arxiv.org/abs/2210.14526>
- Katz, D., Antoja, T., Romero-Gómez, M., et al. 2018, *A&A*, 616, A11, doi: [10.1051/0004-6361/201832865](https://doi.org/10.1051/0004-6361/201832865)
- Kauffmann, G., White, S. D. M., & Guiderdoni, B. 1993, *MNRAS*, 264, 201, doi: [10.1093/mnras/264.1.201](https://doi.org/10.1093/mnras/264.1.201)
- Kim, W.-T., & Ostriker, E. C. 2007, *ApJ*, 660, 1232, doi: [10.1086/513176](https://doi.org/10.1086/513176)
- Kim, W.-T., Seo, W.-Y., Stone, J. M., Yoon, D., & Teuben, P. J. 2012, *ApJ*, 747, 60,
doi: [10.1088/0004-637X/747/1/60](https://doi.org/10.1088/0004-637X/747/1/60)
- Knapen, J. H., Shlosman, I., & Peletier, R. F. 2000, *ApJ*, 529, 93, doi: [10.1086/308266](https://doi.org/10.1086/308266)
- Kraljic, K., Bournaud, F., & Martig, M. 2012, *ApJ*, 757, 60, doi: [10.1088/0004-637X/757/1/60](https://doi.org/10.1088/0004-637X/757/1/60)
- Kwak, S., Kim, W.-T., Rey, S.-C., & Kim, S. 2017, *ApJ*, 839, 24, doi: [10.3847/1538-4357/aa674c](https://doi.org/10.3847/1538-4357/aa674c)
- Laurikainen, E., Salo, H., & Buta, R. 2004, *ApJ*, 607, 103, doi: [10.1086/383462](https://doi.org/10.1086/383462)
- Lee, Y. H., Park, M.-G., Hwang, H. S., et al. 2022, *ApJ*, 926, 58, doi: [10.3847/1538-4357/ac3bc1](https://doi.org/10.3847/1538-4357/ac3bc1)
- Marinova, I., & Jogee, S. 2007, *ApJ*, 659, 1176, doi: [10.1086/512355](https://doi.org/10.1086/512355)
- Marioni, O. F., Abadi, M. G., Gottlöber, S., & Yepes, G. 2022, *MNRAS*, 511, 2423, doi: [10.1093/mnras/stac105](https://doi.org/10.1093/mnras/stac105)
- Martinez-Valpuesta, I., & Gerhard, O. 2011, *ApJL*, 734, L20, doi: [10.1088/2041-8205/734/1/L20](https://doi.org/10.1088/2041-8205/734/1/L20)
- Martinez-Valpuesta, I., Shlosman, I., & Heller, C. 2006, *ApJ*, 637, 214, doi: [10.1086/498338](https://doi.org/10.1086/498338)
- Melvin, T., Masters, K., Lintott, C., et al. 2014, *MNRAS*, 438, 2882, doi: [10.1093/mnras/stt2397](https://doi.org/10.1093/mnras/stt2397)
- Méndez-Abreu, J., Sánchez-Janssen, R., Aguerri, J. A. L., Corsini, E. M., & Zarattini, S. 2012, *ApJL*, 761, L6, doi: [10.1088/2041-8205/761/1/L6](https://doi.org/10.1088/2041-8205/761/1/L6)
- Menéndez-Delmestre, K., Sheth, K., Schinnerer, E., Jarrett, T. H., & Scoville, N. Z. 2007, *ApJ*, 657, 790, doi: [10.1086/511025](https://doi.org/10.1086/511025)
- Naab, T., Oser, L., Emsellem, E., et al. 2014, *MNRAS*, 444, 3357, doi: [10.1093/mnras/stt1919](https://doi.org/10.1093/mnras/stt1919)
- Ness, M., Freeman, K., Athanassoula, E., et al. 2013, *MNRAS*, 432, 2092, doi: [10.1093/mnras/stt533](https://doi.org/10.1093/mnras/stt533)
- Norman, C. A., Sellwood, J. A., & Hasan, H. 1996, *ApJ*, 462, 114, doi: [10.1086/177133](https://doi.org/10.1086/177133)
- Ostriker, J. P., & Peebles, P. J. E. 1973, *ApJ*, 186, 467, doi: [10.1086/152513](https://doi.org/10.1086/152513)
- Pfenniger, D., & Norman, C. 1990, *ApJ*, 363, 391, doi: [10.1086/169352](https://doi.org/10.1086/169352)
- Polyachenko, E. V., Berczik, P., & Just, A. 2016, *MNRAS*, 462, 3727, doi: [10.1093/mnras/stw1907](https://doi.org/10.1093/mnras/stw1907)
- Portail, M., Wegg, C., Gerhard, O., & Ness, M. 2017, *MNRAS*, 470, 1233, doi: [10.1093/mnras/stx1293](https://doi.org/10.1093/mnras/stx1293)
- Quillen, A. C., Minchev, I., Sharma, S., Qin, Y.-J., & Di Matteo, P. 2014, *MNRAS*, 437, 1284, doi: [10.1093/mnras/stt1972](https://doi.org/10.1093/mnras/stt1972)
- Raha, N., Sellwood, J. A., James, R. A., & Kahn, F. D. 1991, *Nature*, 352, 411, doi: [10.1038/352411a0](https://doi.org/10.1038/352411a0)
- Roshan, M., Ghafourian, N., Kashfi, T., et al. 2021, *MNRAS*, 508, 926, doi: [10.1093/mnras/stab2553](https://doi.org/10.1093/mnras/stab2553)
- Saha, K., & Elmegreen, B. 2018, *ApJ*, 858, 24, doi: [10.3847/1538-4357/aabacd](https://doi.org/10.3847/1538-4357/aabacd)
- Salo, H., & Laurikainen, E. 2017, *ApJ*, 835, 252, doi: [10.3847/1538-4357/835/2/252](https://doi.org/10.3847/1538-4357/835/2/252)
- Scannapieco, C., & Athanassoula, E. 2012, *MNRAS*, 425, L10, doi: [10.1111/j.1745-3933.2012.01291.x](https://doi.org/10.1111/j.1745-3933.2012.01291.x)
- Sellwood, J. A. 1980, *A&A*, 89, 296
- . 2014, *Reviews of Modern Physics*, 86, 1, doi: [10.1103/RevModPhys.86.1](https://doi.org/10.1103/RevModPhys.86.1)
- Sellwood, J. A., & Gerhard, O. 2020, *MNRAS*, 495, 3175, doi: [10.1093/mnras/staa1336](https://doi.org/10.1093/mnras/staa1336)

- Sellwood, J. A., & Wilkinson, A. 1993, Reports on Progress in Physics, 56, 173, doi: [10.1088/0034-4885/56/2/001](https://doi.org/10.1088/0034-4885/56/2/001)
- Seo, W.-Y., Kim, W.-T., Kwak, S., et al. 2019, ApJ, 872, 5, doi: [10.3847/1538-4357/aafc5f](https://doi.org/10.3847/1538-4357/aafc5f)
- Sharma, S., Bland-Hawthorn, J., Binney, J., et al. 2014, ApJ, 793, 51, doi: [10.1088/0004-637X/793/1/51](https://doi.org/10.1088/0004-637X/793/1/51)
- Shen, J., Rich, R. M., Kormendy, J., et al. 2010, ApJL, 720, L72, doi: [10.1088/2041-8205/720/1/L72](https://doi.org/10.1088/2041-8205/720/1/L72)
- Shen, J., & Sellwood, J. A. 2004, ApJ, 604, 614, doi: [10.1086/382124](https://doi.org/10.1086/382124)
- Sheth, K., Melbourne, J., Elmegreen, D. M., et al. 2012, ApJ, 758, 136, doi: [10.1088/0004-637X/758/2/136](https://doi.org/10.1088/0004-637X/758/2/136)
- Sheth, K., Elmegreen, D. M., Elmegreen, B. G., et al. 2008, ApJ, 675, 1141, doi: [10.1086/524980](https://doi.org/10.1086/524980)
- Sormani, M. C., Binney, J., & Magorrian, J. 2015, MNRAS, 451, 3437, doi: [10.1093/mnras/stv1135](https://doi.org/10.1093/mnras/stv1135)
- Springel, V., Pakmor, R., Zier, O., & Reinecke, M. 2021, MNRAS, 506, 2871, doi: [10.1093/mnras/stab1855](https://doi.org/10.1093/mnras/stab1855)
- Toomre, A. 1964, ApJ, 139, 1217, doi: [10.1086/147861](https://doi.org/10.1086/147861)
- . 1966, in Geophysical Fluid Dynamics Ref. No. 66-46, ed. W. V. R. Malkus, (Woods Hole, MA: Woods Hole Oceanographic Institute), 111
- . 1981, in The Structure and Evolution of Normal Galaxies (Cambridge:Cambridge Univ.Press)
- Tremaine, S., & Weinberg, M. D. 1984, ApJL, 282, L5, doi: [10.1086/184292](https://doi.org/10.1086/184292)
- Valenzuela, O., & Klypin, A. 2003, MNRAS, 345, 406, doi: [10.1046/j.1365-8711.2003.06947.x](https://doi.org/10.1046/j.1365-8711.2003.06947.x)
- Wegg, C., Gerhard, O., & Portail, M. 2015, MNRAS, 450, 4050, doi: [10.1093/mnras/stv745](https://doi.org/10.1093/mnras/stv745)
- Weinberg, M. D., & Katz, N. 2007, MNRAS, 375, 460, doi: [10.1111/j.1365-2966.2006.11307.x](https://doi.org/10.1111/j.1365-2966.2006.11307.x)
- Whyte, L. F., Abraham, R. G., Merrifield, M. R., et al. 2002, MNRAS, 336, 1281, doi: [10.1046/j.1365-8711.2002.05879.x](https://doi.org/10.1046/j.1365-8711.2002.05879.x)
- Yurin, D., & Springel, V. 2014, MNRAS, 444, 62, doi: [10.1093/mnras/stu1421](https://doi.org/10.1093/mnras/stu1421)
- . 2015, MNRAS, 452, 2367, doi: [10.1093/mnras/stv1454](https://doi.org/10.1093/mnras/stv1454)